Electronic Supplementary Material (ESI) for Energy & Environmental Science.

Supporting Information

Direct Conversion of Thermal Energy to Stored Electrochemical Energy *via* a Self-Charging Pyroelectrochemical Cell

*Tim Kowalchik, Fariha Khan, Danielle Horlacher, Shad Roundy, and Roseanne Warren**

**Corresponding Author: roseanne.warren@utah.edu

PEC Design

PECs were constructed using a glass container and 3D printed components. Figure S1a shows a cell resting in the outer water bath used to apply heating/cooling cycles. Cell temperature was measured using a thermocouple placed within the sealed cell, adjacent to the electrode stack. The cell was sealed with plumber's putty along all air gaps and electrical connections. The cell stack was held in place by a 3D printed clip. A 3D printed wedge was used to prevent vertical movement of either the cell components or the clip. Figure S1b shows each component used, including: lid, clip, wedge, graphite on copper electrodes, and PVDF-BT separator.

No cell was used for more than a week after being built. For prolonged storage (>12 hr), cells were placed in a sealed container and kept at room temperature. No electrodes, separators, or electrolyte were reused after testing, and fresh cells were created for each amperometry and/or OCP experiment.

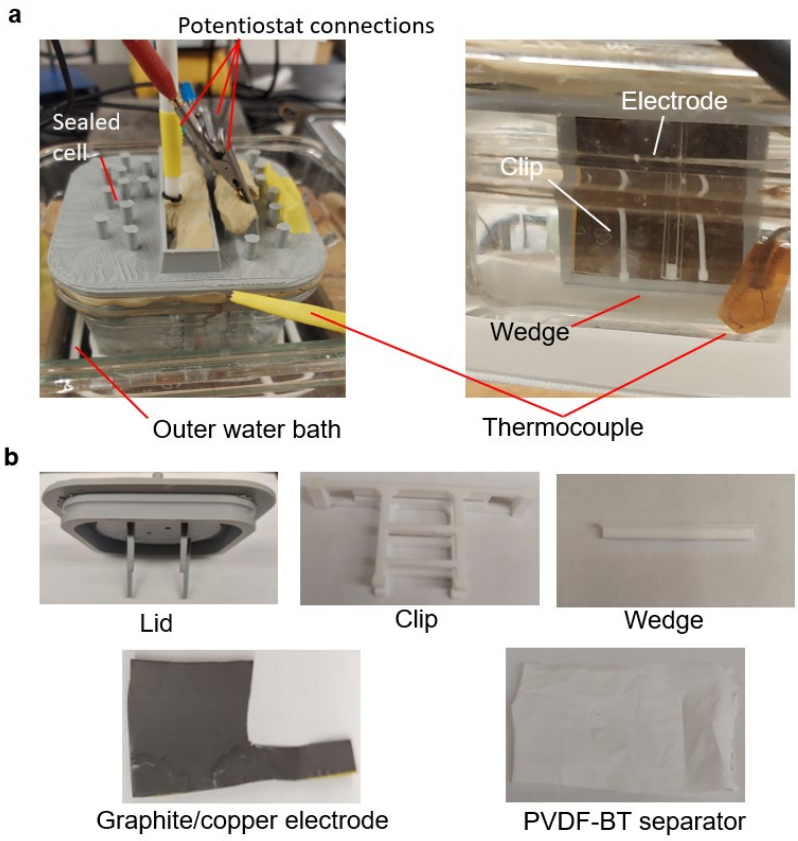

Figure S1. a) Constructed PEC connected to a potentiostat and ready for thermal cycling. Internal components are prevented from moving by the inclusion of a clip and wedge. b) Individual images of: 3D printed lid, clip, and wedge; graphite on copper electrodes; and PVDF-BT separator.

Temperature Profiles Applied During Experimentation and Simulation

Consistent cell temperature ramp profiles were achieved during experiments using a water bath. Table S1 provides specifications for bath water temperatures used during heating and cooling phases, and the corresponding time required for the internal cell temperature to reach the target. In all experiments, water was removed from the bath using a siphon to avoid moving the PEC. Figure S2 plots measured cell temperature *vs.* time profiles for each scenario. In the case of multiple cycling, the same thermal cycle was applied again after the cell returned to 20 °C. Additionally, Figure S2 presents cell temperature *vs.* time profiles corresponding to PEC simulations conducted using COMSOL Multiphysics®. The temperature profiles in COMSOL were calculated based on the heat flux applied to the cell in the model. There is good agreement between experiment and simulation, with only minor differences observed at the onset of the cooling phases for the 20-30-20 °C and 20-50-20 °C thermal cycles. In COMSOL, equal magnitude heat flux profiles can be applied during cooling and heating phases, resulting in symmetric temperature *vs.* time profiles. Such symmetry was not possible during experimentation due to practical limitations achieving sufficiently low bath temperatures during cooling.

Table S1. Thermal cycle specifications.

Thermal cycle	Heat/Cool phases	Bath water temperature (°C)	Time to target temperature (min)	Average dT/dt (°C/min)
20-30-20 °C	H: 20–30 °C	55	17	0.59
	C: 30–20 °C	1	23	-0.44
20-50-20 °C	H: 20–50 °C	85	26	1.15
	C: 50–20 °C	1	34	-0.88
20-10-20 °C	C: 20–10 °C	1	30	-0.33
	H: 10– 20 °C	45	10	1.00

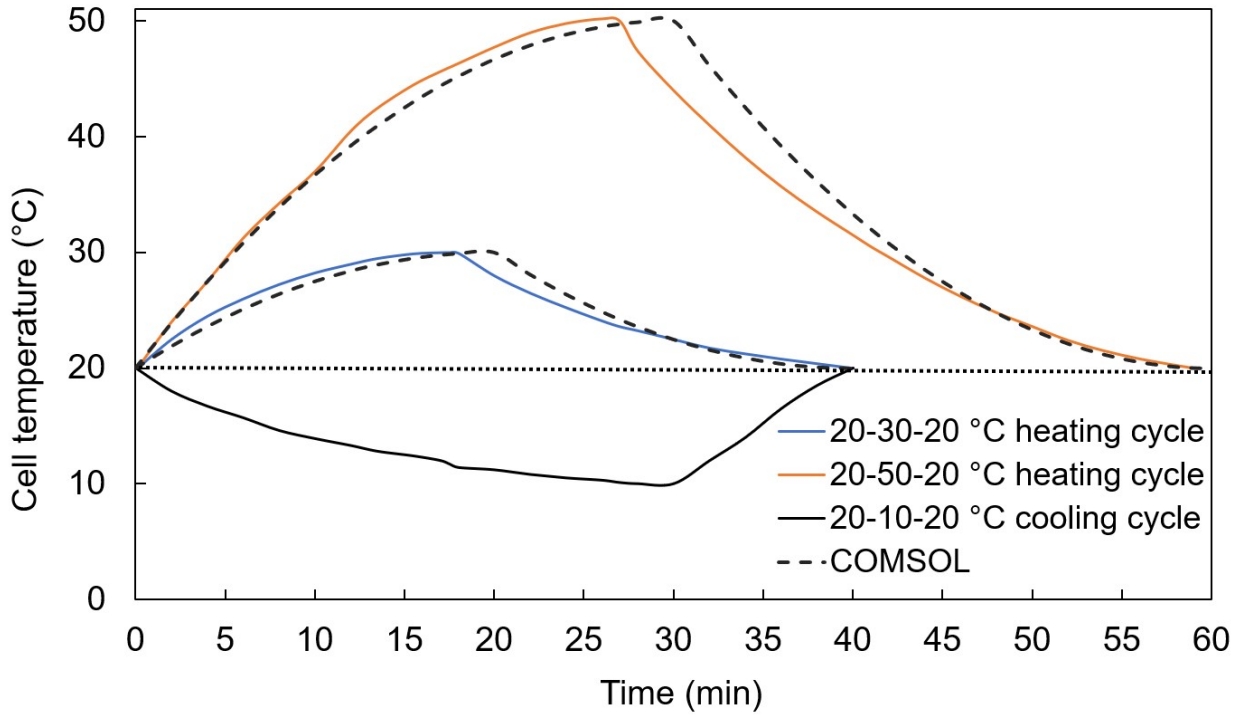

Figure S2. Experimental and simulated cell temperature *vs*. time profiles for thermal cycles 20-30-20 °C, 20-50-20 °C, and 20-10-20 °C.

Experimental Reproducibility

Figure S3 provides an example of experimental reproducibility achieved during thermally cycled amperometry experiments (120 mV, pyroelectric PVDF-BT cell). Between each test, potentiostat leads were removed, reversed, and reconnected, and the water bath conditions changed according to Table S1 (20-30-20 ^{o}C thermal cycle). The results demonstrate a high degree of repeatability, except for Test 1. Differences observed in Test 1 are attributed to cell stabilization. To ensure robust and consistent data analysis, first cycle amperometry results were excluded from the datasets. Tests 2-4 results indicate that methods of disconnecting/reconnecting the potentiostat and thermally cycling the cell do not introduce significant variability in the results.

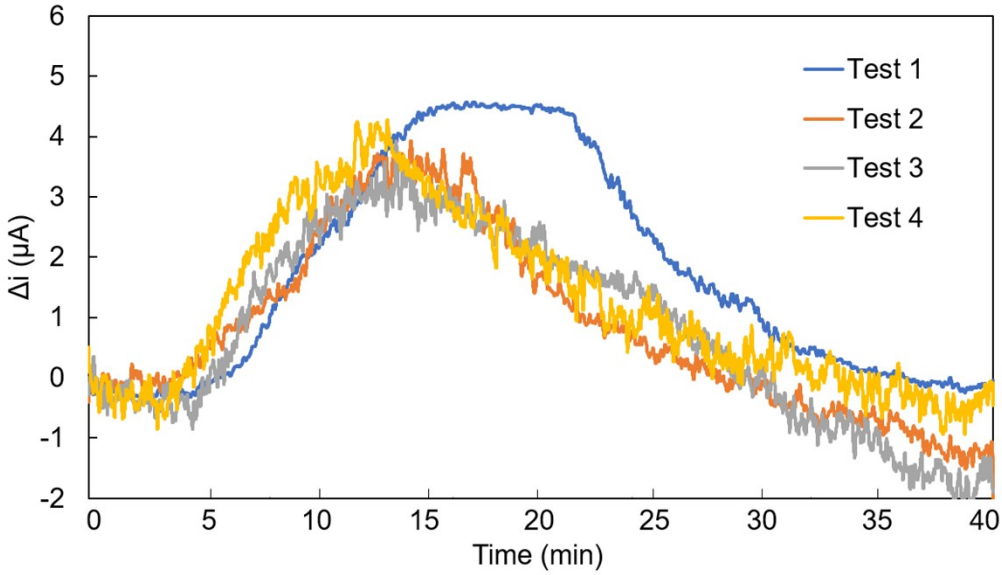

Figure S3. Amperometry measurement of pyroelectric PVDF-BT cell at 120 mV. Change in cell current (Δi) is measured over four 20-30-20 °C thermal cycles (Tests 1-4), with the potentiostat disconnected and reconnected multiple times between each test.

Separator Orientation Methods

Two methods are available to change the pyroelectric orientation relative to the cell cathode and anode: 1) physically reversing the separator, or 2) reversing the potentiostat leads. Physically reversing the separator was found to cause damage to the electrodes over time. Reversing electrode connections is much less damaging to the cells, leading to better repeatability. To ensure these two methods are equivalent, cells were tested with both methods for the same amperometric test (Figure S4). There was excellent consistency in curve shape and magnitude of Δi between flipping the potentiostat leads *vs.* flipping the separator, indicating that the two methods are equivalent for changing the pyroelectric orientation.

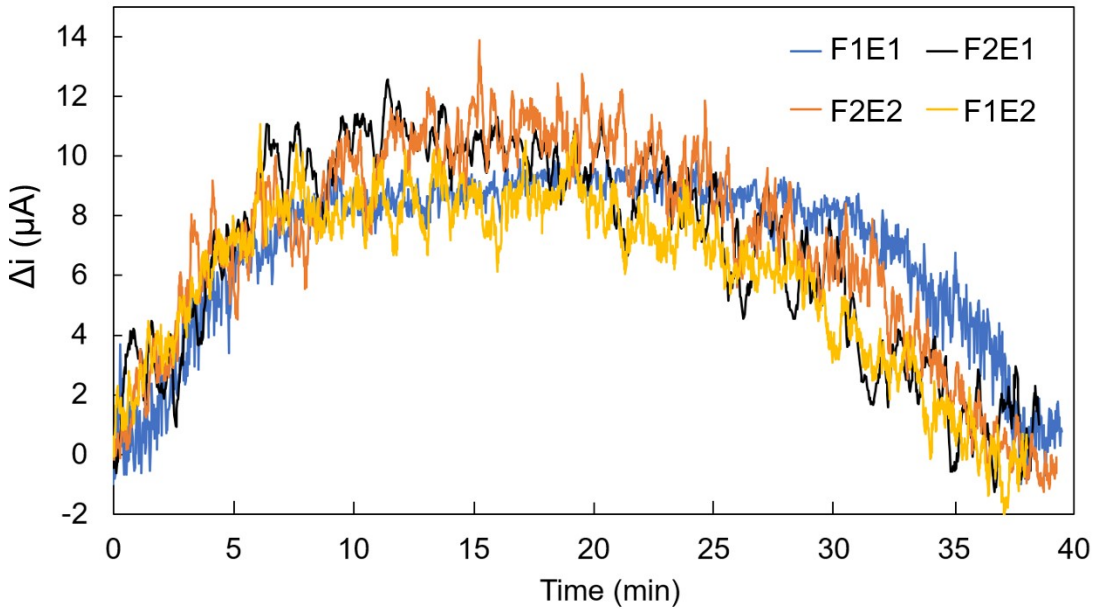

Figure S4. Amperometry tests conducted on a PEC with 20-50-20 °C thermal cycle at 120 mV. "F" denotes physical separator orientation; "E" denotes potentiostat electrode connection. F1E1, F1E2, F2E1 and F2E2 represent all possible combinations of separator and potentiostat lead orientations.

COMSOL Multiphysics® Simulation

Simulation geometry

Figure S5a-c provides details on the 1-D cell geometry employed in COMSOL Multiphysics® simulations. The lengths of each cell region (double layer region, electrolyte, and porous PVDF-BT separator) are specified in Figure S5a. The nodes used in the simulation are shown in Figure S5b. Nodes 1 and 4 represent the surfaces of the PEC graphite electrodes. Since the experimental electrodes are thin, we can expect the potential drop across electrodes and current collector to be small, which allows these components to be modeled as surfaces. No flux conditions were applied at nodes 1 and 4. The separator node, node 3, is a porous media with properties matching those of the PEC separator. BT particles were neglected in the separator physical properties, but accounted for in the pyroelectric properties by means of the experimentally measured pyroelectric coefficient for the PVDF-BT film. The electrolyte was defined on either side of the separator within a single node 2, Both streamline and crosswind diffusion choices were enabled. Figure S5c provides a representation of the meshing density of each region.

Governing physics

Tertiary Current Distribution was selected as the governing physics branch for electrochemistry as it captures detailed information regarding electric double layers. Poisson charge conservation was selected to account for charge separation effects within nanometers of the electrode surfaces. For heat transfer, Heat Transfer in Solids and Fluids was selected as it allows for defining of heat transfer within solids, liquids, and porous media. Figure 5d provides a schematic of the computational sequence employed by the simulation: 1) a heating step is calculated from the heat source, 2) the pyroelectric field is calculated and the components heated, 3) changes in

electrochemistry are calculated, and 4) the cell converges to a solution. This process is repeated until the simulation is finished.

Simulation of experimental tests

Experimental PEC tests were replicated in the simulation as follows. For amperometry: 1) cell voltage was set to 120 mV and the simulation allowed to stabilize for 1600 s; 2) a time-dependent heat input was applied; 3) after the cell reached 20 °C again the simulation was run for another 800 s. For OCP: 1) cell voltage was set to -3.5 mV to replicate average experimental OCP measurements and the simulation allowed to stabilize for 2000 s; 2) five thermal cycles were applied, with 50 s between each cycle.

Solver-specific properties

Quadratic discretization was used for all electrochemistry physics; linear discretization was used for heat transfer physics. A relative tolerance of 0.005 was applied to the solver, with data output at each second. The simulation used a fully coupled Newton method for nonlinear effects, with 40 solver iterations allowed. The direct linear solver used was the MUMPS solver, with 50 iterations allowed for results and a MUMPS pivot threshold of 0.01. Time steps were enforced with the backward differentiation formula (BDF) method, with a maximum time step of 0.5 s and event tolerance of 0.01. The BDF method was set to a maximum order of 2 and minimum order of 1. A crucial component of the time stepping in this work is the initial time step, which was set to 1 μs.

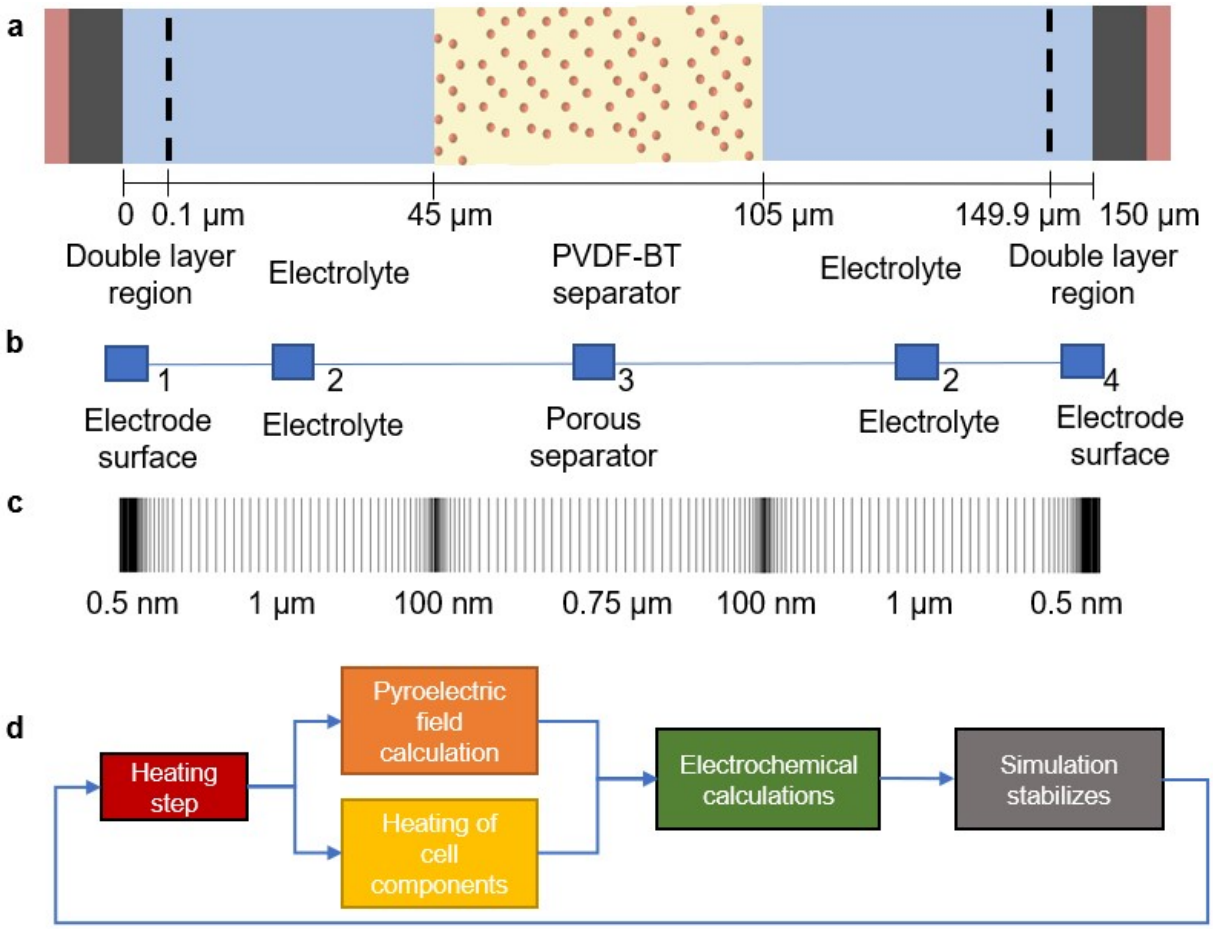

Figure S5. a) Schematic of PEC components employed in the simulation with corresponding *x* coordinates indicated. b) COMSOL nodes used to represent PEC components. c) Representation of the meshing resolution used in the simulation at each region. Near the electrode surfaces and the separator-electrolyte interfaces the meshing is at its greatest density. d) Logic flow of the simulation as each solver step is calculated.

PVDF-BT and Celgard Pyroelectric Response

The pyroelectric response of poled PVDF-BT, unpoled PVDF-BT, and Celgard 3501 films was measured by electroding each film with conductive silver paint. The films were then heated with a heat lamp and the voltage across the film measured. Five samples were measured for each type of separator. Table S2 summarizes the range of peak voltages produced for each separator. Unpoled PVDF-BT exhibits a small pyroelectric response due to remnant polarization from the fabrication process. Both unpoled PVDF and Celgard 3501 films have significantly lower voltage response than poled PVDF-BT.

Table S2. Voltage response of pyroelectric (poled) PVDF-BT, unpoled PVDF-BT, and Celgard 3501 separators employed in this work.

Separator	**Voltage response (mV)**
Poled PVDF-BT	15.1–18.1
Unpoled PVDF-BT	0.2–0.9
Celgard 3501	0.1–0.2

PVDF-BT *vs.* Celgard cell EIS and CV Comparison

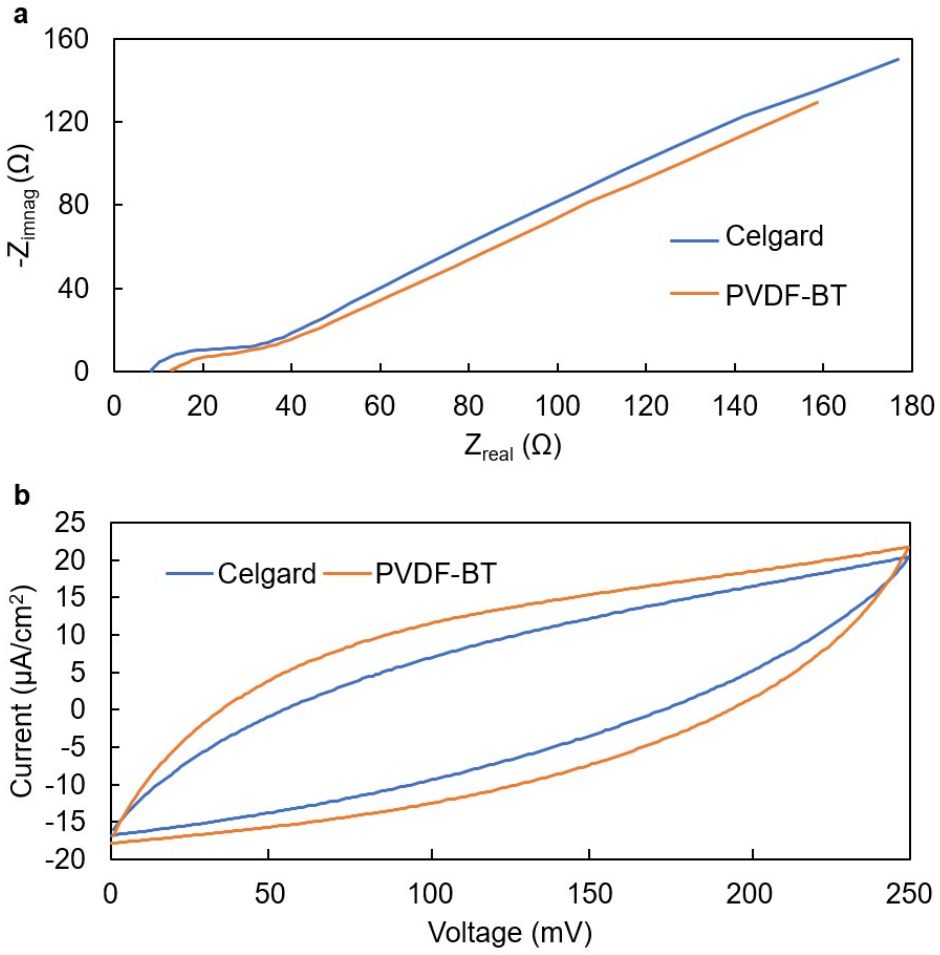

Figure S6. EIS (a) and CV (b) measurements of PECs made with Celgard 3501 *vs.* PVDF-BT separator. All measurements were done at 20 °C. CV measurements were recorded at a scan rate of 100 mV/s.

Experimental Single-Cycle Heating Rate Comparison

For comparison with the simulated heating rate results of Figure 7d, experimental single-cycle OCP testing was conducted for 1x *dT/dt* and 2x *dT/dt* rates (Figure S7). In both cases the cell was heated over a 20-30-20 °C heating cycle. As predicted by our theory of operation, the experimental results show differences in cell OCP *vs*. time for the two heating rates but similar net ΔOCP (0.30 mV for 2x *dT/dt* rate; 0.26 mV for 1x *dT/dt* rate). The maximum ΔOCP for the two heating rates is also similar, as predicted by Equation 2 (1.45 mV for 2x *dT/dt* rate; 1.41 mV for 1x *dT/dt* rate).

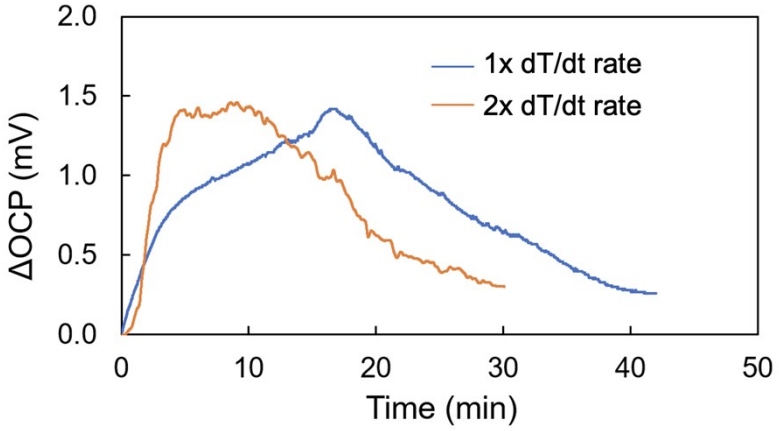

Figure S7. Experimental response of single-cycle OCP testing at different heating rates. 1x *dT/dt* and 2x *dT/dt* rates correspond to those used in simulations (Figure 7d), applied over a 20-30-20 °C heating cycle.

Self-Charging Power Cell Performance Comparison

Table S3 compares open circuit voltage, energy and/or power production values reported in literature for self-charging power cells with PEC results reported in this study. Due to the limited exploration of self-charging devices in general, and the large variability in results reporting, obtaining energy production values for direct comparisons between devices is challenging. Despite these limitations, Table S3 clearly indicates that the PEC device reported in this work (a first-generation demonstration) achieves power density values comparable to more well-developed, widely studied technologies such as thermogalvanic cells.

Table S3. Self-charging power cell performance comparison.

Author, Year	Energy harvested	Cell description	Performance result
Xue et al., 2012 [1]	Piezoelectric	Piezoelectric self-charging power cell; $LiCoO_2$ cathode, TiO_2 anode, piezoelectric PVDF separator powered through compression.	68 mV, 0.036 μAh[(a)]
Ramadoss et al., 2015 [2]	Piezoelectric	Piezoelectric self-charging power cell; MnO_2 electrodes, PVDF-ZnO piezoelectric separator.	110 mV [(b)]
Li et al., 2021 [3]	Thermogalvanic	Zinc ion thermogalvanic cell for low grade thermal energy harvesting; Cathode VO_2-PC, Zn anode.	1.2 mW max, 10 μW/cm^2 [(c)]
Yu et al., 2019 [4]	Thermogalvanic	Thermogalvanic cell combined with Cu foam heat sink and PPy heat exchanger; graphite electrode sheets with $K_4Fe(CN)_6/K_3Fe(CN)_6$ electrolyte.	0.6 W/m^2 ideal, 1.3-8.3 μW/cm^2 [(d)]
Ding et al., 2019 [5]	Regenerative electrochemical cell	Solar-driven isothermal regenerative electrochemical cell; $K_4Fe(CN)_6/K_3Fe(CN)_6$ catholyte, KI/KI_3 anolyte, rGO wrapped carbon felt current collector.	41.6 mV, 33.2 μW/cm^2 [(e)]
This work	Pyroelectric	Pyroelectric self-charging power cell; C electrode, pyroelectric PVDF-BT separator powered through environmental temperature changes	4.89 μW/cm^2 [(f)]

a) Cell works through replacing the separator of a Li-ion battery coin cell with piezoactive PVDF to drive ions in response to the piezoelectric voltage. A partially charged cell at 327 mV was charged through repeated compressions up to 395 mV over 240 s, then discharged at 1 μA over 130 s giving the reported stored energy value of 0.036 μAh. No reported area or power densities.

b) A continuation of the work in [1], this self-charging cell used piezoelectricity from compression to charge a symmetric electrochemical cell. Compressed by pressing on the device with a palm, voltage increased from 35 mV to 145 mV over 300 s. No reported energy or power densities.

c) Cell powered through thermo-extraction/insertion and thermodiffusion on the cathode and stripping/plating on the anode. No reported area; $\mu W/cm^2$ value in Table S4 estimated roughly from images of the cell and reported max power of one cell under a temperature difference of 45 °C.

d) Device consists of a thermogalvanic cell combined with a faster heat exchange layer on one electrode and a heat sink on the other. During the day the faster heating creates a temperature difference across the cell. At night the heat sink releases thermal energy in the opposite direction. A power density of 0.6 W/m^2 was reported using artificial light simulating a temperature difference of 40 °C on an unknown device area. Sunlight testing provided 0.13 mW at night and 0.83 mW during the day with a reported area of 100 cm^2 which was used to calculate the power density in Table S3.

e) Cuvette-based cell testing utilizing the rGO wrapped carbon felt to create a more effective solar absorption. Artificial sunlight used to create a temperature cycle of 30 °C to 65 °C with the reported power density.

f) PEC device of this work. Power estimated by taking average ΔOCP per cycle of 0.65 mV (Figure 7) and PEC resistance (24 Ω) along with area (36 cm^2).

Thermal Energy Harvester Performance

Table S4 shows selected open circuit voltage, energy and/or power production values reported in literature for other thermal energy harvesting devices besides self-charging cells. Thermal harvesting can be accomplished through a variety of methods, with output power ranging from μW's to W's depending on the source and harvester.

Table S4. Selected thermal energy harvester performance comparison.

Author, Year	Energy harvested	Device description	Performance result
Xu et al., 2022 [6]	Solar	Solar-driven thermal evaporation of seawater; copper coated sponges in water beds	117.8 mV, 25 nA
Yap et al., 2016 [7]	Thermoelectric	Body-heat thermoelectric generator; commercial thermoelectric generator	150 mV, 30 $\mu W/cm^2$
Waske et al., 2019 [8]	Thermomagnetic	Thermomagnetic generator; magnetocaloric parallel plates	1.24 mW
Goswami et al., 2020 [9]	Thermoelectric	Biomass waste-heat powered thermoelectric generator; thermosyphon system coupled with biomass gasifier	0.615 W

Leakage Current Assessment

a. PEC leakage current estimation

Leakage current is an important consideration in the design and implementation of IoT energy harvesting and storage devices. Amperometry measurements conducted at constant temperature provide a preliminary estimate of PEC leakage current. At room temperature, PECs held at 120 mV had an average current draw of 1.56 $\mu A/cm^2$ after 20 minutes (pre-thermal cycling). This corresponds approximately to the leakage current of the device. The actual leakage current of the PEC measured after 72 hours is expected to be less than this value. Assuming a typical charge management circuit current consumption of 0.5 μA, the PEC must achieve a minimum of 0.25 $\mu W/cm^2$ thermal-to-electrochemical energy conversion to achieve a net charging effect at this voltage.[10] In OCP testing, the estimated energy conversion of the PEC is 4.86 $\mu W/cm^2$. From these estimates, we conclude that it is possible to achieve net charging of the PEC when leakage current is considered. A typical IoT use case is characterized by a short-term active mode and a long inactive sleep mode. This affords opportunity for continuous thermal charging of the PEC over multiple charge cycles while the sleep mode current draw is low.

b. Temperature effects

Supercapacitor leakage current is known to increase with temperature. While the exact temperature dependence varies significantly with device design (*e.g.* electrode materials, electrolyte) and temperature range of operation, a general rule-of-thumb suggests that leakage current doubles for every 10 ^oC increase in temperature.[11] Figure 5 provides proof-of-concept of the PEC operating with a cooling cycle instead of a heating cycle. These results suggest that there may be opportunities to reduce leakage current effects in PEC devices compared to other thermal energy harvesters by charging the device in "cooling mode".

c. Opportunities for leakage current reduction

Finally, we note that there are a variety of techniques for reducing leakage current in supercapacitors that may be implemented in future studies of PEC devices. Individual supercapacitor components may be modified with several techniques to reduce leakage current.[12] Electrolyte concentration may reduce leakage by more than 10x.[13] Power-management circuitry can lead to a >90% reduction in lost energy over the course of a week.[14] Optimization of wireless sensor power draw improves efficiency and reduces losses.[15] Many of these techniques may be applied to the PEC in future work, which we predict will be able to lower leakage current substantially based on available literature. Combined with increasing PEC energy production, practical devices operational in a wide range of environmental applications may be obtained.

References:

[1] X. Xue, S. Wang, W. Guo, Y. Zhang, Z. L. Wang, Hybridizing energy conversion and storage in a mechanical-to-electrochemical process for self-charging power cell. Nano Lett. 2012, 12, nl302879t.

[2] A. Ramadoss, B. Saravanakumar, S. W. Lee, Y. Kim, S. J. Kim, Z. L. Wang, Piezoelectric-driven self-charging supercapacitor power cell. ACS Nano 2015, 9, 5b00759.

[3] Z. Li, Y. Xu, L. Wu, Y. An, Y. Sun, T. Meng, H. Dou, Y. Xuan, X. Zhang, Zinc ion thermal charging cell for low-grade heat conversion and energy storage. Nat. Comm. 2022, 13, s41467.

[4] B. Yu, J. Duan, J. Li, W. Xie, H. Jin, R. Liu, H. Wang, L. Huang, B. Hu, J. Zhou, All-day thermogalvanic cells for environmental thermal energy harvesting. Research 2019, 2460953.

[5] Y. Ding, X. Guo, K. Meyers, Y. Zhou, L. Zhang, F. Zhao, G. Yu, Simultaneous energy harvesting and storage via solar-driven regenerative electrochemical cycles. Energy Envir. Sci. 2019, 12, C9EE01930H.

[6] Y. Xu, J. Xu, J. Zhang, X. Li, B. Fu, C. Song, W. Shang, P. Tao, T. Deng, All-in-one polymer sponge composite 3D evaporators for simultaneous high-flux solar-thermal desalination and electricity generation. Nano Energy 2022, 93, 106882.

[7] Y. Yap, R. Naayagi, W. Woo, Thermoelectric energy harvesting for mobile phone charging application. IEEE TENCON 2016, 7848649.

[8] A. Waske, D. Dzekan, K. Sellschopp, D. Berger, A. Stork, K. Nielsch, S. Fahler, Energy harvesting near room temperature using a thermomagnetic generator with a pretzel-like magnetic flux topology. Nat. Energy 2018, 4, s41560

[9] R. Goswami, R. Das, Waste heat recovery from a biomass heat engine for thermoelectric power generation using two-phase thermosyphons. Renew. Energy 202, 148, 2019.10.067.

[10] X. Yue, J. Keily, D. Gibson, E. M. Drakakis, Charge-based supercapacitor storage estimation for indoor sub-mW photovoltaic energy harvesting powered wireless sensor nodes. IEEE Trans. Indust. Elec. 2020, 67, 2896321.

[11] B. E. Conway, Electrochemical supercapacitors, Springer, New York, NY, USA 1999.

[12] K. Liu, C. Yu, W. Guo, L. Ni, J. Yu, Y. Xie, Z. Wang, Y. Ren, J. Qui, Recent research advances of self-discharge in supercapacitors: Mechanisms and suppressing strategies. J. Energy Chem. 2021, 58, 2020.09.041.

[13] M. Shi, Z. Zhang, M. Zhao, X. Lu, Z. L. Wang, Reducing the self-discharge rate of supercapacitors by suppressing electron transfer in the electric double layer. J. Electrochem. Soc. 2021, 168, ac44b9.

[14] Q. Ju, Y. Zhang, Reducing charge redistribution loss for supercapacitor-operated energy harvesting wireless sensor nodes. In 2nd Int. Workshop Energy Neutral Sensing Sys. 2014, 2675691.

[15] A. Abuellil, J. J. Lopez, A. Bommireddipalli, A. Reyes, Z. Zeng, E. Sinencio, Multiple-input harvesting power management unit with enhanced boosting scheme for IoT applications. IEEE Trans. Indust. Elec. 2020, 67, 2920607.